www.czasopisma.pan.pl PAN POLSKA AKADEMIA NAUK www.journals.pan.pl

ARCHIVES OF ACOUSTICS Online First October 17, 2024 doi: 10.24425/aoa.2024.148815

Research Paper

Prediction Method and Characteristics of Static Acoustic Scattering for Marine Composite Propellers

Suchen XU[(1)], Zilong PENG[(1)*], Fulin ZHOU[(2)], Xuhong MIU[(3)], Huicheng KE[(1)]

[(1)] *School of Energy and Power*
Jiangsu University of Science and Technology
Zhenjiang, China

[(2)] *State Key Laboratory of Ocean Engineering*
Collaborative Innovation Center for Advanced Ship and Deep-Sea Exploration
Shanghai Jiao Tong University
Shanghai, China

[(3)] *Unit 92578 of the People's Liberation Army*
Beijing, China

*Corresponding Author e-mail: zlp_just@sina.com

(*received May 10, 2024; accepted July 4, 2024; published online October 17, 2024*)

This study introduces a hybrid approach to predict the acoustic scattering characteristics of composite propellers featuring variable thickness and complex curvature. The approach combines the Kirchhoff approximation (KA), which employs an intersection algorithm (IA) for determining the thickness of discrete surface elements, with the theory of orthotropic laminate transfer matrix (OLTM). The overall scattered sound field of the target is determined by solving the reflection coefficients of each surface element. To enhance computational efficiency, the scattered sound field of a complete composite propeller is ingeniously predicted by cloning mesh topology from a single propeller blade, taking advantage of the rotation symmetry characteristics of the composite propeller. The validity of this prediction method is confirmed through the finite element method (FEM) and static acoustic scattering characteristic experiments conducted on a lake. The predicted results for the target strength (TS) of the composite propeller closely align with the FEM. Additionally, the TS and time-domain echo characteristics of the steel propeller utilizing the KA exhibit strong agreement with the experimental findings. These research findings provide a significant reference value for predicting the acoustic scattering characteristics near the stern of underwater vehicles.

Keywords: acoustic scattering characteristics; composite propeller; Kirchhoff approximation; target strength.

1. Introduction

When active sonar is utilized to detect the stern of an underwater vehicle, the stern sections, including the propeller, and the rudder, contribute the main echo (CHU, STANTON, 2010; KLAUSNER, AZIMI-SADJADI, 2014; TUCKER, AZIMI-SADJADI, 2011). Compared to traditional metal propellers, composites offer advantages such as higher strength, lower specific gravity, corrosion resistance, and good capability of stealth (VARDHAN *et al.*, 2019; ISLAM *et al.*, 2022; UDDIN *et al.*, 2021; MOTLEY *et al.*, 2009). However, the acoustic scattering characteristics of the composite propeller are often overlooked in both domestically and internationally research. Modeling the acoustic response of static non motion propellers primarily focuses on their inherent acoustic characteristics in a non-working state, analyzing how material properties and geometric shapes influence acoustic scattering characteristics. In contrast, modeling the acoustic response of rotat-

ing propellers primarily addresses the hydrodynamic noise generated during operation, which is more complex than static propeller modeling. This involves accounting for the Doppler frequency shift effect induced by rotation and the acoustic scattering characteristics of the wake bubble cloud (Cheng *et al.*, 2023; Saffari *et al.*, 2023). For a static composite propeller, it is crucial to consider variations in blade thickness and curvature.

Currently, prevalent numerical methods for predicting the acoustic scattering characteristics of underwater targets at low frequencies include the finite element method – FEM (Jiang *et al.*, 2023; Isakson, Chotiros, 2014; Sabat *et al.*, 2023; Yang *et al.*, 2024), and the boundary element method – BEM (Langdon, Chandler-Wilde, 2006; Venås, Kvamsdal, 2020; Seybert *et al.*, 1988; Zhang *et al.*, 2020). However, these numerical methods necessitate significant computational resources, with increasing frequency. The Kirfchhoff approximation (KA) method is extensively employed for rapid prediction of the acoustic scattering characteristics of complex targets in a high-frequency range (Kwon *et al.*, 2017). Lavia *et al.* (2019) discretized the target into individual curved surface elements and computed the target's backscattering in high frequency through iterative integration using the Gauss-Legendre rule, as adopted in the KA. Tang *et al.* (1993) proposed a method called the planar element method, which has been broadly utilized in modeling acoustic echo of complex targets.

Numerous issues persist when employing the KA method for analyzing the acoustic scattering characteristics of the composite propeller. Each discrete surface element of a propeller blade possesses the distinct thickness and curvature (Sagar *et al.*, 2013), with the primary variation pattern characterized by thinning towards the edges and thickening towards the leading edge, as well as transitioning from thicker at the blade root to thinner at the blade tip. The traditional KA method, used for assessing target strength (TS), only considers the reflection coefficients of uniformly thick targets. Variations in thickness and curvature across different parts of blades, as well as complex edge profiles, which inevitably lead to computational errors, have not yet been taken into account.

In this paper, a predictive method for the acoustic scattering characteristics of composite thin plates with variable thickness is proposed. By constructing discrete element thickness and material property information, and based on the theory of orthotropic laminate transfer matrix (OLTM), the reflection coefficients of all elements are solved. This leads to the acquisition of the total scattered sound field for composite targets with variable thickness. By employing a mesh cloning topology approach, the prediction of acoustic scattering characteristic for the composite propeller with rotational symmetry structures has been realized. The accuracy of this method in predicting the acoustic scattering characteristics of the static composite propeller has been validated through the FEM. Finally, this method is applied to the isotropic steel propeller, where the predicted results of TS and time-domain echo characteristics are in good agreement with experimental results.

2. Theoretical research

2.1. Physical method of geometrical acoustic scattering of underwater target

The KA formula is applied to the problem of acoustic scattering on nonrigid surfaces, as shown in Fig. 1. *Oxyz* denotes a spatial Cartesian coordinate system, S represents the integral surface of the nonrigid target, Q_1 is the point of sound wave incidence, and Q_2 is the point of sound wave reception. The vectors $\mathbf{r}_1$ and $\mathbf{r}_2$ correspond to the positions of the incidence and reception points, respectively; α_1 and α_2 are the angles of incidence and reception, respectively, while $\mathbf{n}$ represents the normal vector of the surface element.

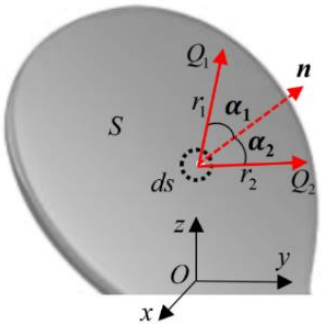

Fig. 1. Schematic diagram of the integral region.

Assume that the surface reflection coefficient is $V(\alpha)$ and the surface acoustic impedance is Z. In the illuminated region, the elastic surface conditions are:

$$\begin{cases} \phi_s = V(\alpha)\phi_i, \\ \dfrac{i\omega\rho_0(\phi_i+\phi_s)}{\partial(\phi_i+\phi_s)/\partial\mathbf{n}} = -Z, \end{cases} \tag{1}$$

where ϕ_i and ϕ_s are the potential functions of the incident sound wave and the scattered sound field, respectively, ω is the angular frequency of the incident wave, and ρ_0 is the density of the medium surrounding the target. From this, the potential function of the scattered sound wave is obtained as follows (Fan *et al.*, 2012):

$$\phi_s = -\frac{ikA}{4\pi}\int_S \frac{e^{ik(\mathbf{r}_1+\mathbf{r}_2)}}{\mathbf{r}_1\mathbf{r}_2}V(\alpha)(\cos\alpha_1+\cos\alpha_2)\mathrm{d}s, \tag{2}$$

where k is the sound wavenumber, A is the amplitude.

In monostatic configuration,

$$\mathbf{r}_1 = \mathbf{r}_2 = \mathbf{r},$$

$$\alpha_1 = \alpha_2 = \alpha,$$

it follows that:

$$\phi_s = -\frac{ikA}{2\pi}\int_S \frac{e^{2ik\mathbf{r}}}{\mathbf{r}^2} V(\alpha)\cos\alpha\,\mathrm{d}s. \tag{3}$$

The TS under the far-field conditions is obtained as follows:

$$\mathrm{TS} = 10\lg\left(\frac{1}{\lambda^2}|I|^2\right), \tag{4}$$

where λ is the sound wavelength,

$$I = \int_S e^{2ik\Delta r}\cos\alpha V(\alpha)\,\mathrm{d}s,$$

and Δr is the path difference of a surface element relative to a reference point.

2.2. Theory of orthotropic laminate transfer matrix

The physical model for the propagation of plane waves in composite laminated plates is shown in Fig. 2. θ_i is the angle of incidence, θ_r is the angle of reflection, and θ_t is the angle of transmission, with the angular frequency denoted as ω. The x_3 refers to the direction of thickness, while x_1 refers to the principal direction. For a given single-layer medium, the x_3 coordinate of the transmission boundary is 0, and the x_3 coordinate of the incident boundary is d_k, representing the thickness of that layer. The total thickness D of the multi-layered solid medium is

$$D = \sum_{k=1}^{n} d_k.$$

Fluid media are present on both sides of the composite laminated plate. At the fluid-solid interface, the wave type conversion occurs: part of the wave is reflected into the external fluid, while the remainder converts into shear and longitudinal waves, continuing to propagate in the orthotropic medium and undergoing further reflection and transmission at the lower interface.

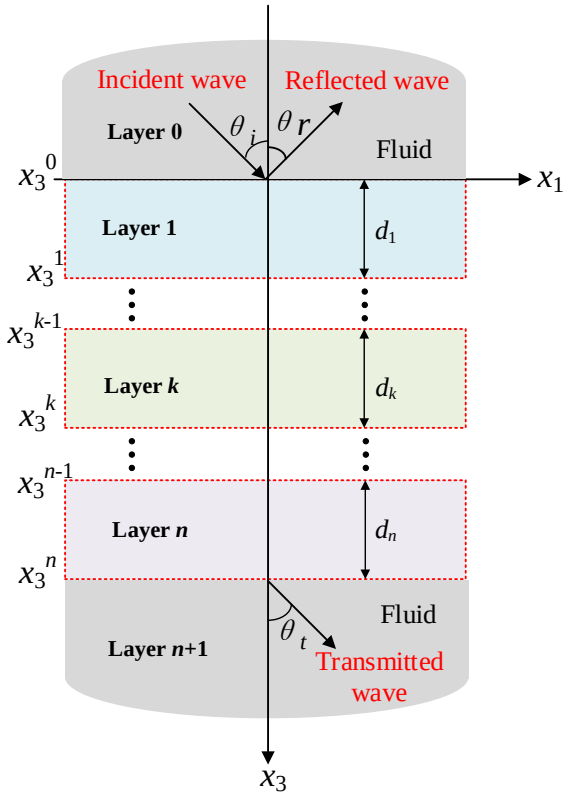

Fig. 2. Schematic diagram of interface between fluid and solid.

According to the theory of OLTM (Kuo *et al.*, 2008; Lin *et al.*, 2017), the relationship between stress, vibrational velocity, and amplitude in a single uniform medium is:

$$\begin{bmatrix} v_1 \\ v_3 \\ \sigma_{33} \\ \sigma_{13} \end{bmatrix} = [M] \begin{bmatrix} (R_1 + R_1') \\ (R_1 - R_1') \\ (R_2 + R_2') \\ (R_2 - R_2') \end{bmatrix}, \tag{5}$$

where v_1 and v_3 are the velocity of x_1 and x_3 direction, respectively; σ_{33} and σ_{13}, respectively, are the normal stress and shear stress on the solid surface; R_1 and R_2 are the amplitudes of the incident sound wave, while R_1' and R_2' are the amplitudes of the reflected sound wave.

The matrix $\mathbf{M}$ is:

$$[M] = \begin{bmatrix} \omega k_t \cos(k_{13}x_3) & -j\omega k_t \sin(k_{13}x_3) & j\omega k_{23}\sin(k_{23}x_3) & -j\omega k_{23}\cos(k_{23}x_3) \\ -j\omega_{13}\sin(k_{13}x_3) & \omega k_{13}\cos(k_{13}x_3) & \omega k_t \cos(k_{23}x_3) & -j\omega k_t \sin(k_{23}x_3) \\ -(Q_{13}k_t^2 + Q_{33}k_{13}^2)\cos(k_{13}x_3) & j(Q_{13}k_t^2 + Q_{33}k_{13}^2)\sin(k_{13}x_3) & j(Q_{33}-Q_{13})k_t k_{23}\sin(k_{23}x_3) & -(Q_{33}-Q_{13})k_t k_{23}\cos(k_{23}x_3) \\ 2jQ_{55}k_t k_{13}\sin(k_{13}x_3) & -2Q_{55}k_t k_{13}\cos(k_{13}x_3) & Q_{55}(k_{23}^2 - k_t^2)\cos(k_{23}x_3) & -jQ_{55}(k_{23}^2 - k_t^2)\sin(k_{23}x_3) \end{bmatrix}, \tag{6}$$

where Q_{ij} is the element of the stiffness matrix for orthotropic materials (Li, 2022); k_t is the wave number of the incident sound wave along the tangential direction of the plate; k_{13} and k_{23} are the compression wave and the shear wave in the direction of x_3, respectively.

$$k_t = \frac{\omega}{c_0}\sin\theta_i, \tag{7}$$

$$k_{13} = \sqrt{\frac{\omega^2 - A_1 k_t^2}{A_3}} = \omega\sqrt{1 - \frac{A_1}{c_0^2}\sin^2\theta_i/A_3}, \tag{8}$$

$$k_{23} = \sqrt{\frac{\omega^2 - a_1 k_t^2}{a_3}} = \omega\sqrt{1 - \frac{a_1}{c_0^2}\sin^2\theta_i/a_3}, \tag{9}$$

where c_0 is the sound speed of fluid; $A_1 = (Q_{11} + Q_{13} + 2Q_{55})/2\rho$ and $A_3 = (Q_{33} + Q_{13} + 2Q_{55})/2\rho$; $a_1 = (Q_{11} - Q_{13})/2\rho$ and $a_3 = (Q_{33} - Q_{13})/2\rho$; ρ is the material density.

At the incident boundary, $x_3 = d$, while at the transmission boundary, $x_3 = 0$. Therefore, the mutual transfer relationships of vibrational velocity and stress at the upper and lower surfaces of each layer of the medium is:

$$\begin{bmatrix} v_1 \\ v_3 \\ \sigma_{33} \\ \sigma_{13} \end{bmatrix}\Bigg|_D = [M_d][M_0]^{-1}\begin{bmatrix} v_1 \\ v_3 \\ \sigma_{33} \\ \sigma_{13} \end{bmatrix}\Bigg|_0 = [TT_k]\begin{bmatrix} v_1 \\ v_3 \\ \sigma_{33} \\ \sigma_{13} \end{bmatrix}\Bigg|_0, \tag{10}$$

where $[TT_k]$ is the stress-strain transfer matrix of the layer no. k of the medium.

At the interfaces between different solid media, the stress and strain are continuous and consistent. Therefore, based on the consecutive multiplication of matrix, the overall transfer matrix $[T]$ of stress and vibrational velocity from the transmission boundary to the incident boundary of the multi-layered medium is:

$$\begin{bmatrix} v_1 \\ v_3 \\ \sigma_{33} \\ \sigma_{13} \end{bmatrix}\Bigg|_D = \prod_{k=1}^{n}[TT_k]\begin{bmatrix} v_1 \\ v_3 \\ \sigma_{33} \\ \sigma_{13} \end{bmatrix}\Bigg|_0 = [T]\begin{bmatrix} v_1 \\ v_3 \\ \sigma_{33} \\ \sigma_{13} \end{bmatrix}\Bigg|_0. \tag{11}$$

Applying the conditions of normal stress and normal displacement continuity on the upper and lower surfaces of orthotropic laminated plates (Hu, 2017), the reflection coefficient R and the transmission coefficient D can be expressed as:

$$R = \frac{jk_{13}^{n+1}(a^*) - (b^*)\omega^2\rho_{n+1}}{jk_{13}^{n+1}(a^*) + (b^*)\omega^2\rho_{n+1}}, \tag{12}$$

$$D = \frac{\rho_1}{\rho_{n+1}}\frac{jk_{13}^{n+1}(1-R)}{jk_{13}^1 m_{22} + m_{23}\rho_1\omega^2}, \tag{13}$$

where

$$a^* = jm_{32}k_{13}^1 + m_{33}\rho_1\omega^2,$$

$$b^* = jm_{22}k_{13}^1 + m_{23}\rho_1\omega^2,$$

ρ_1 and ρ_{n+1} are the fluid medium density at the incident and transmission boundaries, respectively; k_{13}^1 and k_{13}^{n+1} are the wave numbers of the compressional wave at the incident and transmission boundaries, respectively; $m_{ik} = T_{ik} - T_{i1}T_{4k}/T_{41}$,

$$k_{13}^1 = \frac{\omega}{c_0}\cos\theta_i, \tag{14}$$

$$k_{13}^{n+1} = \frac{\omega}{c_0}\cos\theta_t. \tag{15}$$

2.3. Calculation method for static acoustic scattering of the composite propeller

For addressing the acoustic scattering issues of the composite propeller, a method is proposed that involves independent assessing and assigning values to the thickness of discrete surface elements during the KA process.

For the issue of element thickness discrimination, a simplified judgment method is proposed: the thickness determination of each independent element can be approximated as a problem of solving the spatial vector length at point M_2 of the rear interface plate penetrated by the normal located at the central point O_1 of the front plate. The spatial vectors from the origin to points O_1 and M_2 are represented as $\mathbf{O}_1$ and $\mathbf{M}_2$, respectively, and the length of this vector is the thickness d of the plate, the method for determining the thickness of an element is shown in Fig. 3.

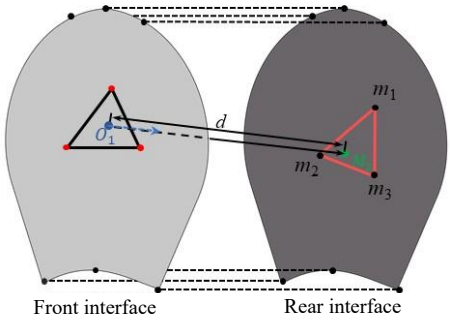

Fig. 3. Method for determining the thickness of surface elements.

Based on the intersection algorithm – IA (Möller, Trumbore, 1997), $\mathbf{M}_2(uv)$ can be defined and represented as $\mathbf{M}_2(u,v) = \mathbf{O}_1 + \mathrm{d}\mathbf{n}$, with the assumption that:

$$\mathbf{O}_1 + \mathrm{d}\mathbf{n} = (1-u-v)\,\mathbf{m}_1 + u\mathbf{m}_2 + v\mathbf{m}_3, \tag{16}$$

where u and v satisfy the conditions: $u \geq 0$, $v \geq 0$, and $u + v = 1$; $\mathbf{m}_1$, $\mathbf{m}_2$, $\mathbf{m}_3$, respectively, represent the spatial position vectors of the vertices of the rear plate, the normalized vector in the direction of the normal of the front plate is $\mathbf{n}$. After organizing, it is obtained that:

$$\begin{bmatrix} -\mathbf{n} & \mathbf{m}_2 - \mathbf{m}_1 & \mathbf{m}_3 - \mathbf{m}_1 \end{bmatrix}\begin{bmatrix} d \\ u \\ v \end{bmatrix} = \mathbf{O}_1 - \mathbf{m}_1. \tag{17}$$

Move the vertex $\mathbf{m}_1$ of the rear interface element to the origin and transform it into a unit triangle within the Oyz plane, aligning the normal direction $\mathbf{n}$ parallel to the x-axis. Define $\mathbf{E}_1 = \mathbf{m}_2 - \mathbf{m}_1$, $\mathbf{E}_2 = \mathbf{m}_3 - \mathbf{m}_1$, $\mathbf{T} = \mathbf{O}_1 - \mathbf{m}_1$, by applying Cramer's rule to Eq. (17), the solution is obtained as follows:

$$\begin{bmatrix} d \\ u \\ v \end{bmatrix} = \frac{1}{(\mathbf{n} \times \mathbf{E}_2) \cdot \mathbf{E}_1} \begin{bmatrix} (\mathbf{T} \times \mathbf{E}_1) \cdot \mathbf{E}_2 \\ (\mathbf{n} \times \mathbf{E}_2) \cdot \mathbf{T} \\ (\mathbf{T} \times \mathbf{E}_1) \cdot \mathbf{n} \end{bmatrix}. \tag{18}$$

The element thickness d can be determined by solving Eq. (18).

A mesh cloning topology method is proposed for rotationally symmetric structures to predict the acoustic scattering characteristics of multiple propeller blades. This is achieved by applying planar rotational operations to the mesh nodes of a single propeller blade within the same plane, thereby expanding it into a multi-blade mesh. The complete model mesh is then obtained through topological methods. This method is shown in Fig. 4. P_1, P_2, and P_3 represent the original mesh vertices, while P_1', P_2', and P_3' represent the mesh vertices after topology, with $\mathbf{a}$ representing the spatial vector from the origin to point P_1, and $\mathbf{b}$ representing the spatial vector from the origin to point P_1'.

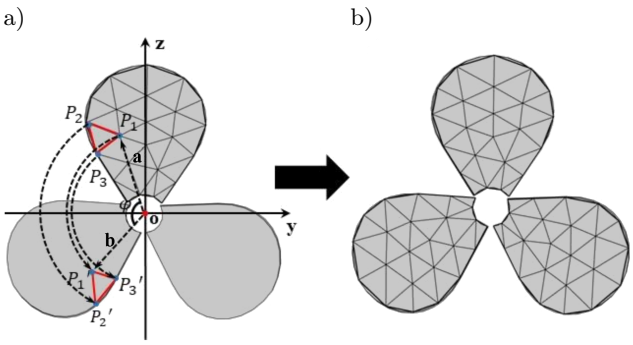

Fig. 4. Mesh cloning topology method: a) shows the topology process; b) shows the mesh after topology.

When cloning a single propeller blade to obtain three blades, the mesh rotates around the axis of 120°. Connect P_1 with the origin O of the coordinate axis to obtain the vector $\mathbf{a} = (y, z)$. The line connecting O and P_2, which is obtained by rotating P_1, forms the vector $\mathbf{b} = (y', z')$. By applying Eqs. (19)–(21), the rapid calculation of y' and z' can be realized, thereby obtaining the mesh node information for the three-blade propeller:

$$\cos\varphi = \frac{\mathbf{a} \cdot \mathbf{b}}{|\mathbf{a}||\mathbf{b}|}, \qquad \varphi = 120°, \tag{19}$$

$$-\frac{1}{2} = \frac{yy' + zz'}{\sqrt{y^2 + z^2}\sqrt{y'^2 + z'^2}}, \tag{20}$$

$$y' = \frac{-y \pm \sqrt{3}z}{2}, \qquad z' = \frac{\sqrt{3}y \pm z}{2}. \tag{21}$$

2.4. Research on time-domain echo characteristics of target

In the framework of linear acoustics, the problem of target scattering can be described using an acoustic transfer theory. The target can be regarded as a linear time-invariant network. In this network, the incident signal is the input, and the echo signal is the output. The time-domain transfer function of this linear transfer network is $h(\tau, \mathbf{r}_1, \mathbf{r}_2, \rho)$, where τ is the delay, $\mathbf{r}_1$ and $\mathbf{r}_2$ are the radius vectors of the incident and scattering points, respectively, and ρ is the radius vector of the target. The frequency domain transfer function $H(f, \mathbf{r}_1, \mathbf{r}_2, \rho)$ of the transfer network is denoted as the ratio of the scattering wave potential function to the incident wave potential function, where f is frequency. In the monostatic configuration, there is $\mathbf{r}_1 = \mathbf{r}_2$, and the transfer functions in the time-domain and frequency domain are $h(\tau, \mathbf{r}, \rho)$ and $H(f, \mathbf{r}, \rho)$, respectively.

When $x(t)$ represents the time-domain incident signal, $X(f)$ represents the frequency domain incident signal, and $Y(f)$ represents the frequency domain echo signal. The time-domain echo signal of the target can be expressed as:

$$y(t) = x(t) \otimes h(\tau, \mathbf{r}, \rho), \tag{22}$$

where $\otimes$ is convolution operation, then the echo signal in the frequency domain is given by:

$$Y(f) = X(f) \cdot H(f, \mathbf{r}, \rho), \tag{23}$$

$$y(t) = F^{-1}[Y(f)]. \tag{24}$$

The time-domain echo signal can be obtained by taking the inverse Fourier transform of the frequency domain signal. This theory allows for the indirect extraction of the time-domain echo characteristics of underwater targets by calculating the frequency domain signals.

3. Simulation calculation and model

3.1. Composite propeller model

The computational model is a composite propeller of underwater vehicles, comprising a hub and blades. The propeller is made of carbon fiber, with its primary material parameters outlined in Table 1 (Jing *et al.*, 2022). The basic dimensional parameters of the propeller are presented in Table 2.

In Table 1, E_1 is the longitudinal elastic modulus; E_2 and E_3 are the transverse elastic moduli; v_{12}, v_{23}, and v_{13} are the Poisson ratios in the 12, 23, and 13 directions, respectively; G_{12}, G_{23}, and G_{13} are the shear moduli in the 12, 23, and 13 directions, respectively; ρ is the density.

Table 1. Material parameter.

Parameter	Numerical value
E_1 [GPa]	140
E_2 [GPa]	9
E_3 [GPa]	9
v_{12}	0.32
v_{23}	0.46
v_{13}	0.32
G_{12} [GPa]	4.6
G_{23} [GPa]	3.08
G_{13} [GPa]	4.6
ρ [kg/m^3]	1620

Table 2. Basic parameters of propeller.

Parameter	Numerical value
Tip circle radius [mm]	261.5
Disk ratio	0.507
Number of blades	3
Propeller rake angle [°]	0
Hub diameter shape	linear type
Hub bore diameter [mm]	67
Hub outside diameter [mm]	81

Due to the unique design of the blade, which feature a larger thickness near the hub and along the midline of the blade surface, and a gradual decrease in thickness towards the blade edges and along the radial direction, the radial thickness variations of the propeller blade model are significant. Therefore, measurements of the sectional profile dimensions at different radial distances of a single blade are conducted. The construction of the blade model and the selected radial positions of the sections are shown in Fig. 5. In the figure, R represents the tip circle diameter.

Using traditional methods to measure propeller dimensions (Zhu, 2020), it is assumed that the generatrix is a curve located at a specific point along the longitudinal direction of the propeller blade. This curve rotates around the propeller axis while moving axially, thus forming the three-dimensional surface of the propeller blade. The generatrix OH located in the middle of the blade surface is selected as the reference line, serving as the benchmark for measuring the shape and size of the propeller blade. The maximum thickness variation of the blade section is obtained from the blade section projection diagram. Table 3 illustrates the relative positional relationship of points on the blade camber line and the trailing edge line of section at different radii ranging from $0.2R$ to $0.95R$.

Table 3. Single blade section profile dimensions.

r/R	Distance from the generatrix to the leading edge [mm]	Sectional chord length [mm]	Sectional perimeter [mm]	Maximum sectional thickness [mm]
0.2	67.58	135.16	274.41	7.55
0.3	82.27	164.53	332.93	6.45
0.4	97.76	195.51	394.77	5.54
0.5	109.13	218.25	440.80	4.80
0.6	113.25	226.50	458.10	4.20
0.7	110.15	220.30	446.24	3.69
0.8	98.56	197.12	401.30	3.23
0.9	74.26	148.51	302.45	2.80
0.95	52.71	105.42	215.95	2.58
1.0	–	–	–	2.00

Measurements of certain parameters under a single blade's top and upward view are conducted, with the specific parameters detailed in Table 4.

Table 4. Partial parameters of a single-blade propeller.

Parameter [mm]	Numerical value
$a_{\max}$	206
c_1	10
c_2	2
d_1	88

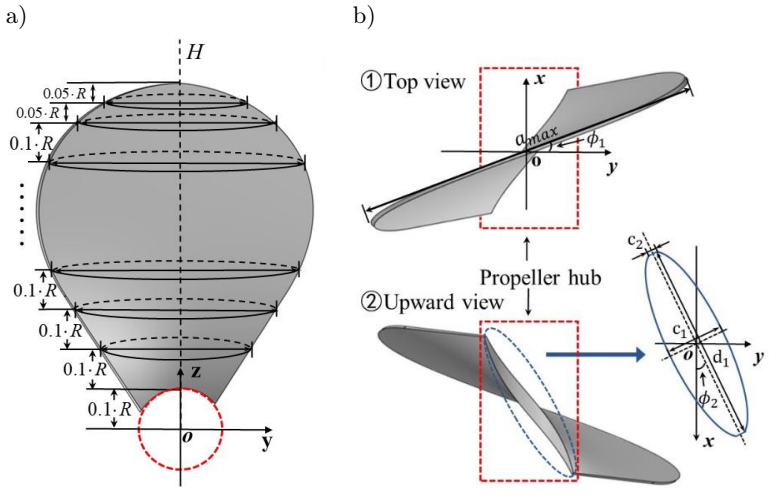

Fig. 5. Single blade structure: a) shows the front view; b) shows the top and upward views.

Measurements are taken of the outer edge of the blade root cross-section in Fig. 6b, combining circular curves and line segments to draw the lower sectional profile, ϕ_1 and ϕ_2 represent the rotational scales of the upper and lower sections, respectively, both set at 20°. By selecting cross-sectional profiles at multiple radial distances, the basic dimensions of the blade's shape are determined, completing the overall propeller blade construction.

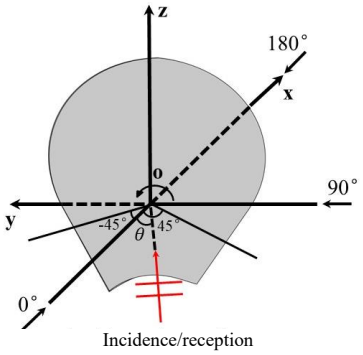

Fig. 6. Schematic diagram of model calculation angle.

3.2. Acoustic scattering characteristics of a single composite propeller blade

The acoustic scattering characteristics of a single composite propeller blade are simulated using finite element software, employing acoustic-solid coupling in the frequency domain for an underwater single composite propeller blade.

In simulations of the scattering acoustic field of a single composite propeller blade using the COMSOL FEM simulation software, the perfect matching layer (PML) technology is introduced to simulate the boundary conditions of an infinite free field. This technology serves as an absorbing boundary, preventing sound waves from reflecting at the interface between the conventional internal computation domain and the PML. This simulation solutions are compared with the KA method. Figure 6 presents the angle setting diagram, the schematic diagram for calculating acoustic scattering of a single composite propeller blade. Figure 7 illustrates a schematic diagram of the FEM calculation model.

The simulation model is established with water as the fluid medium and the incident sound wave

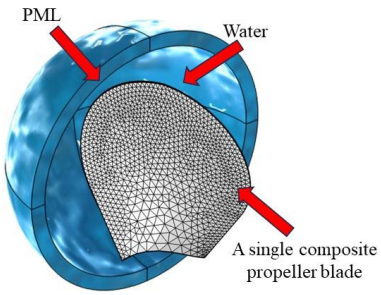

Fig. 7. FEM calculation model of a single composite propeller blade.

as a plane wave. The angle θ between the incident wave in the *Oxy* plane and the negative half-axis of the x-axis is considered. Two methods, the FEM and the KA, with a thickness variation interval ranging from 2 mm to 7.55 mm, are employed for comparative analysis of the TS. Figure 8 shows the directivity diagrams of TS at different frequencies, with θ ranging from 0° to 360° in 2° intervals (omnidirectional scattering). Figure 9 compares the directivity diagrams of TS at different frequencies, with an incident angle θ of −45° to 45° and a step size of 1° (forward scattering).

Figures 8 and 9 demonstrate that the KA method is largely consistent with the FEM results and offers a significant advantage in computation time. Table 5 provides the times required to compute the TS.

3.3. Acoustic scattering characteristics of the composite propeller

The acoustic scattering characteristics of the complete propeller model, derived from mesh cloning topology of a single propeller blade, are calculated. The TS results for the composite propeller are compared using both the KA and the FEM. The coordinate origin is centered at the propeller hub disk, with the incident wave direction at 0° perpendicular to the propeller hub disk. Calculation angles, θ, are set to range from 0° to 360° in 2° intervals. The comparison of the directivity diagrams of TS is shown in Fig. 10. The overall TS for the composite propeller, which includes multiple blades and the central hub, is obtained through the coherent superposition of the scattered sound fields, with the hub portion considered as a rigid target in the calculations. Table 6 presents the time required to compute the TS.

Table 5. Comparison of time required for TS calculation.

Omnidirectional scattering and forward scattering	FEM/KA	Number of mesh elements	Number of mesh nodes	Calculation time [s]
Omnidirectional scattering	FEM	192303	41910	2150.5
	KA	22396	11200	393.15
Forward scattering	FEM	192303	41910	2034.1
	KA	22396	11200	394.64

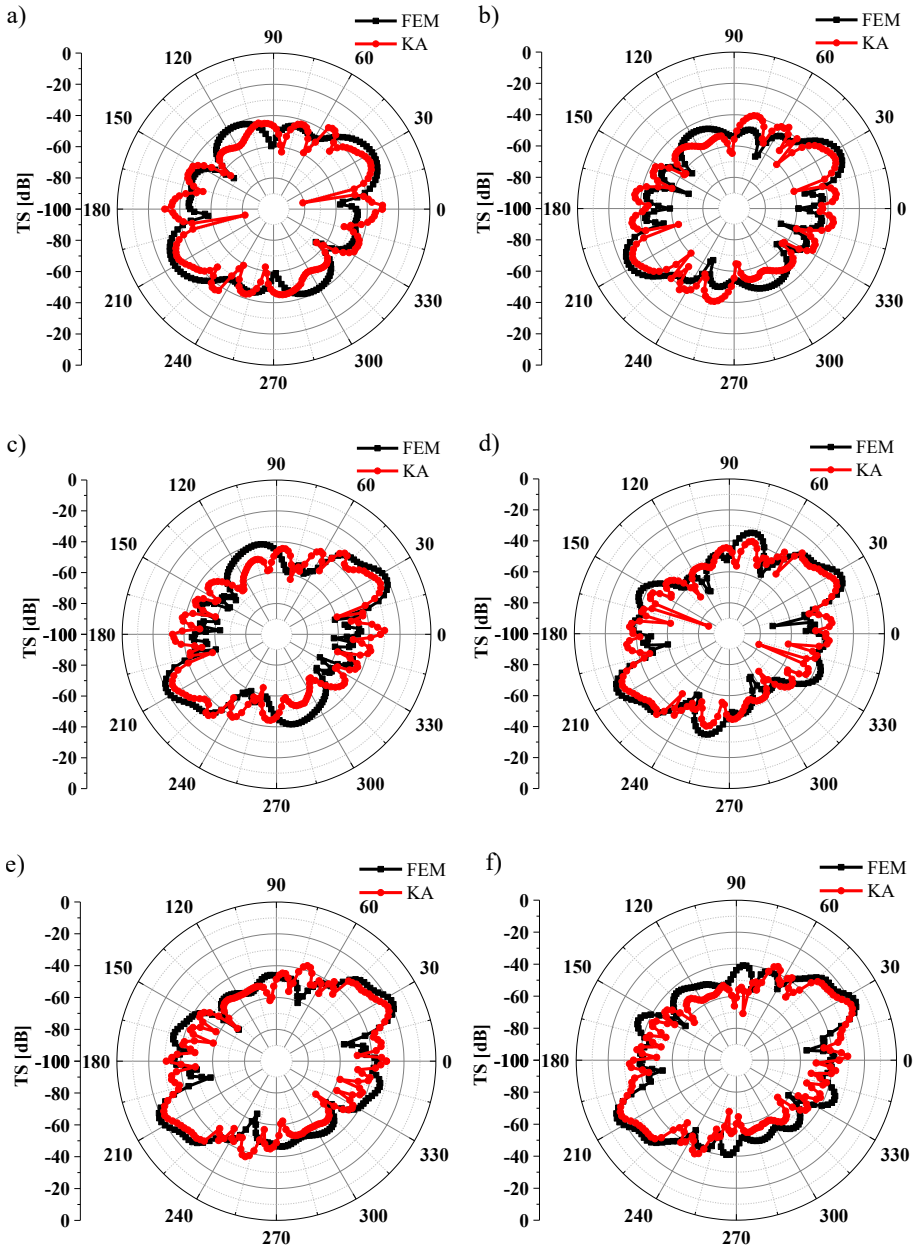

Fig. 8. Comparison of omnidirectional scattering TS for a single composite propeller blade at different frequencies: a) 12 kHz; b) 16 kHz; c) 21 kHz; d) 24 kHz; e) 26 kHz; f) 29 kHz.

Table 6. Comparison of time required for TS calculation.

FEM/KA	Number of mesh elements	Number of mesh nodes	Calculation time [s]
FEM	1503875	292033	16069.8
KA	80867	40645	877.7

As indicated in Fig. 10, the results from the KA are largely consistent with those of the FEM, especially in the forward and aft scattering regions (θ at 0° to 30° and 150° to 210°) at high frequencies. However, at certain oblique incident angles, discrepancies are observed due to the TS derived from the coherent superposition of the hub and blades, which diverges from the unified calculations of a complete model.

The comparison with the FEM results reveals that for the composite propeller, a rotationally symmetric structure, the directivity diagrams of TS exhibit a rotationally symmetric distribution as well. Peaks oc-

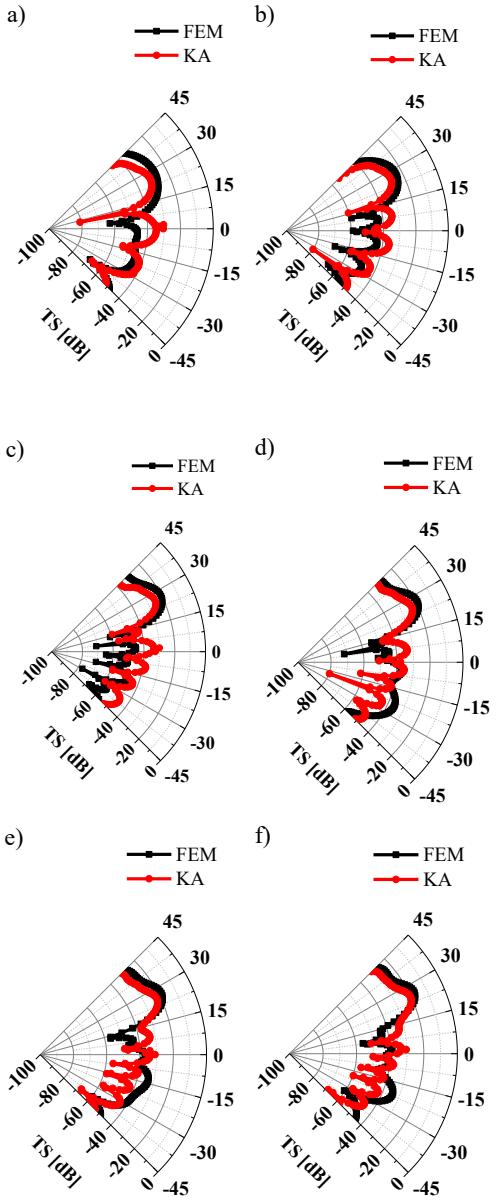

Fig. 9. Comparison of forward scattering TS for a single composite propeller blade at different frequencies: a) 12 kHz; b) 16 kHz; c) 21 kHz; d) 24 kHz; e) 26 kHz; f) 29 kHz.

cur in the 20° to 40° and 200° to 220° ranges, with strong TS regions near 30° and 210°. These are primarily due to the contributions from multiple composite propeller blades, where the unique inclined angle of the blades causes many normal vectors of surface elements to align almost parallel to the incident wave direction at these angles. As Eq. (12) indicates, an increase in the incident wave frequency enhances the reflection coefficient on the composite propeller blade surface, leading to more pronounced directivity within this angular range. Significant fluctuations in TS with multiple peaks are observed in the 0° to 30°, 75° to 105°, 150° to 210°, and 255° to 285° ranges. These are attributed to the contributions from the annular end face of the hub and some bright areas on the blades. Echo interference from different parts of the composite propeller occurs, and the plane structure acoustic scattering characteristics of the propeller hub disk are significantly influenced by the angle.

3.4. Comparison between composite and steel propellers

The accuracy of the KA method was validated through comparison with the FEM. This was achieved by contrasting TS of the composite propellers with that of the steel propeller and analyzing the acoustical modulation effect of composite materials. Frequency computations were conducted within the range of 10 kHz to 30 kHz with a step size of 200 Hz, while an-

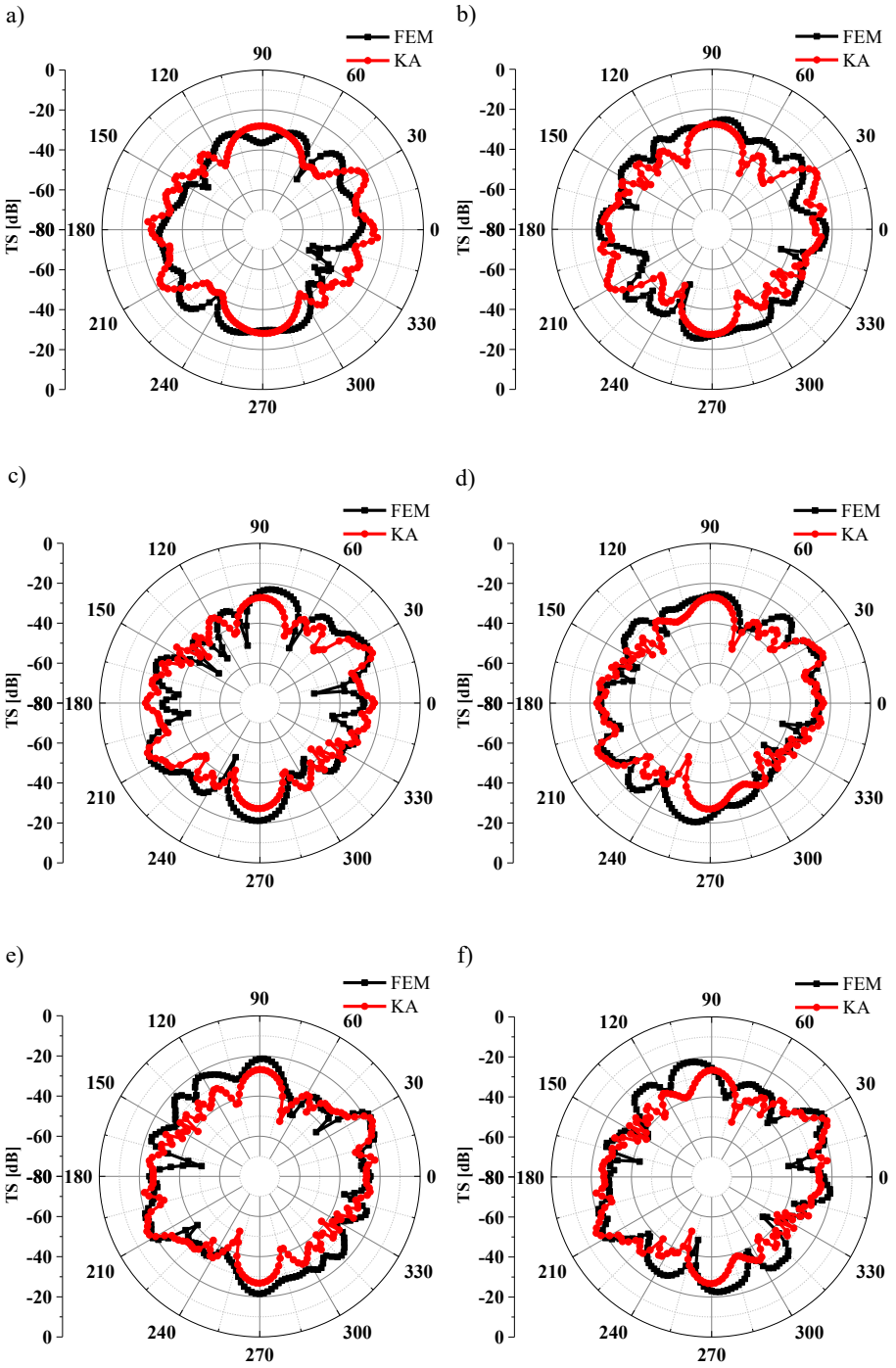

Fig. 10. Comparison of TS for composite propellers at different frequencies:
a) 12 kHz; b) 17 kHz; c) 20 kHz; d) 21 kHz; e) 23 kHz; f) 24 kHz; g) 27 kHz; h) 29 kHz.

gle variations were assessed from 0° to 360° with a step size of 2°. In Fig. 11, the horizontal axis represents the incident angle of the sound wave, which the vertical axis denotes the incident frequency of the sound wave.

According to Figs. 11 and 12, compared to the steel propeller, the composite propeller exhibits a significant decrease in TS predominantly within the angular range of 15° to 45° and 195° to 225°. This reduction is attributed to the parallel alignment between the normal vectors of discrete elements and the direction of sound waves within these angular intervals, which enhances the reflection coefficient of the composite materials, thereby facilitating effective acoustical modulation. However, with an increase in frequency, leading to the reduction in the wavelength of the sound waves, the extent of reduction in TS diminishes.

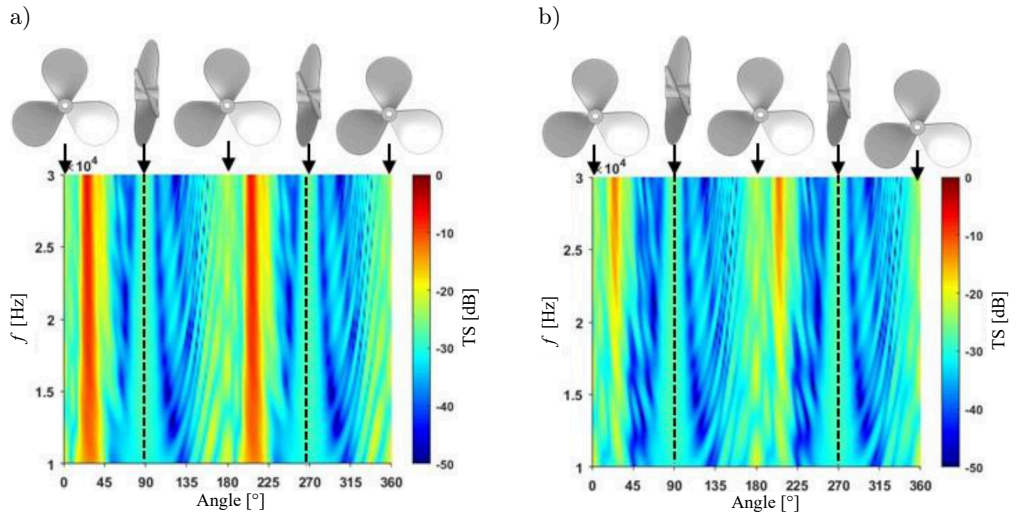

Fig. 11. Comparison of TS: a) shows TS of the steel propeller; b) shows TS of the composite propeller.

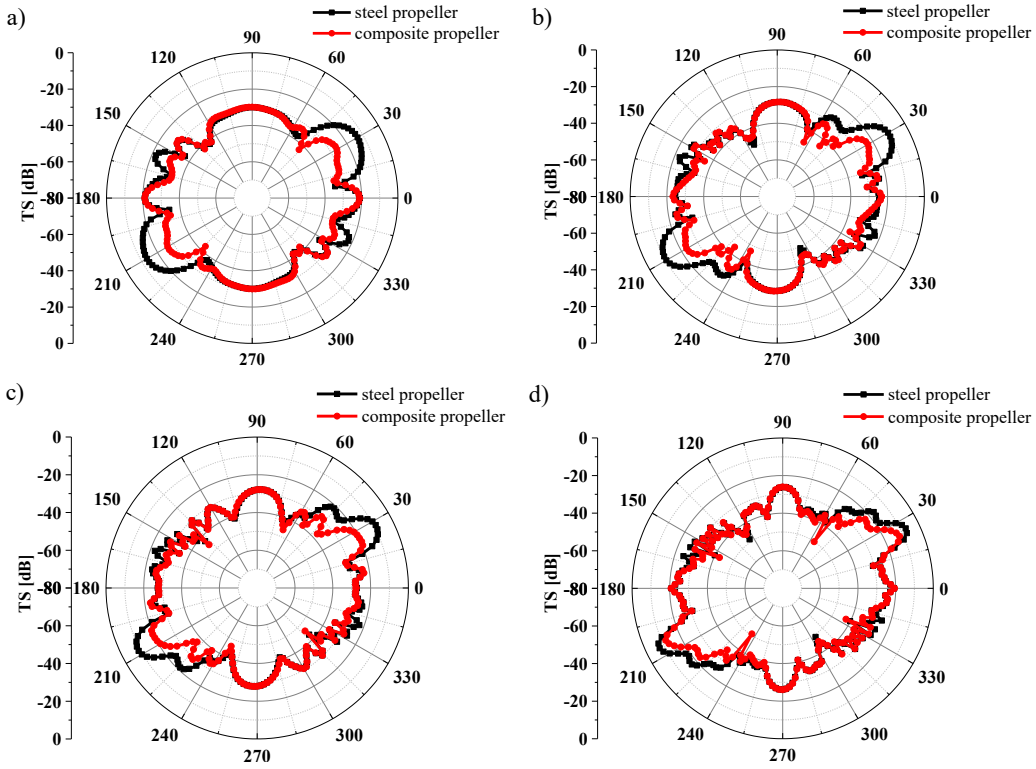

Fig. 12. Comparison of TS between steel propeller and composite propeller at different frequencies: a) 10 kHz; b) 15 kHz; c) 20 kHz; d) 30 kHz.

4. Comparison of acoustic scattering characteristics between the KA solutions and experimental results

4.1. Acoustic scattering characteristic experiment instrument and arrangement

Due to the demanding processing requirements and lengthy production cycles associated with composite material propellers, steel propellers, which are isotropic and can be considered as special cases of orthotropic materials, offer a more universal option. Verification of the KA method suffices for these materials. Thus, a lake experiment on scaled models of steel propellers was conducted to verify this approach. By analyzing the echo characteristics of the steel propeller in relation to variations in incident angles and frequencies, this experiment provides essential data to support the accuracy of predictive methods for TS in the thin plate target with variable thickness.

The primary material parameters used include a density of 7800 kg/m^3, Poisson's ratio of 0.3, and Young's modulus of 2.1×10^{11} Pa. Figure 13 shows the steel propeller scale model.

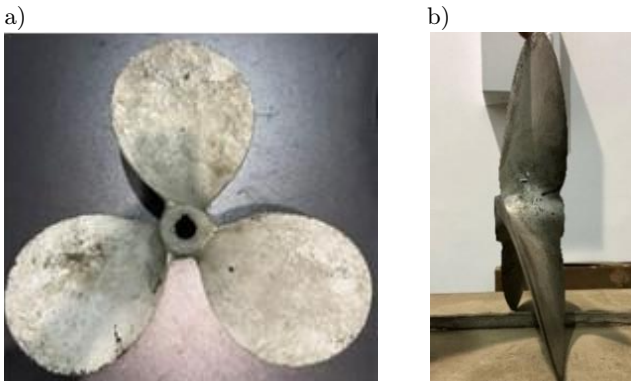

Fig. 13. Steel propeller experiment model: a) shows the front view; b) shows the side view.

Figure 14 is a schematic diagram of the experiment equipment arrangement. The transducer, hydrophone, and detection target are positioned at the same depth. This depth, measured from the water surface, is 7.38 m. The distance between the transducer and the hydrophone is 3.65 m, while the distance between the hydrophone and the measurement target is 3.32 m. During the measurement process, the propeller rotates uniformly underwater in a suspended posture, with a rotation angle ranging from 0° to 360°.

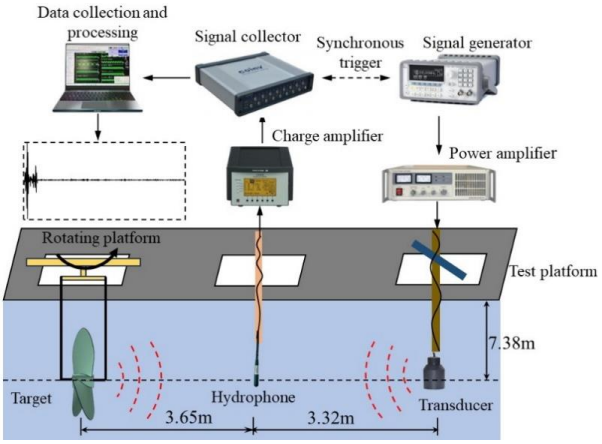

Fig. 14. Schematic diagram of the experiment equipment arrangement.

4.2. Experimental data analysis of the time-domain echo characteristics of the steel propeller scale model

In the experiment, a scaled steel propeller model was utilized. Incident acoustic waves were directed at the model across a full 360° range. These signals were linear frequency modulated pulses, spanning a frequency band of 10 kHz to 20 kHz with a pulse width of 3 ms. The geometric center of the incidence setup was aligned with the hub disk center of the propeller, ensuring that the incident wave vector faced the center of the propeller hub disk directly at 0° incidence. The time-domain echo characteristics obtained from the experiment were then compared with the KA solutions as shown in the Fig. 15. The horizontal axis represents the attitude azimuth angle of the model, which the vertical axis denotes the moment of the echo.

From Fig. 15, it is evident that strong echo bright spots are pronounced near the 30° and 210°. Both the experimental findings and the KA solutions reveal a similar distribution pattern of these bright spots, indicating a close correlation in their variation trends. This similarity suggests that the propeller blades' side inclination angle plays a crucial role in the echo characteristics, especially when analyzing the time-domain acoustic scattering characteristics of the steel propeller. However, some discrepancies between the experimental data and the KA method predictions persist. These differences might stem from small size of the model, which could lead to weaker echo signals at the receiving point. Additionally, experimental limitations may have hindered accurate observation of the underwater model's posture, potentially causing instability at certain angles and, consequently, inaccuracies in the results.

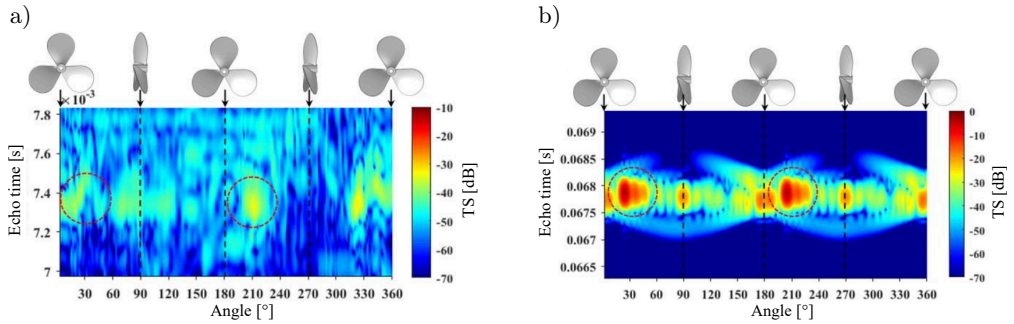

Fig. 15. Comparisons of the echo characteristics of the steel propeller scale model in the frequency band of 10 kHz–20 kHz between the experimental results and KA solutions: a) shows the experimental results; b) shows the KA solutions.

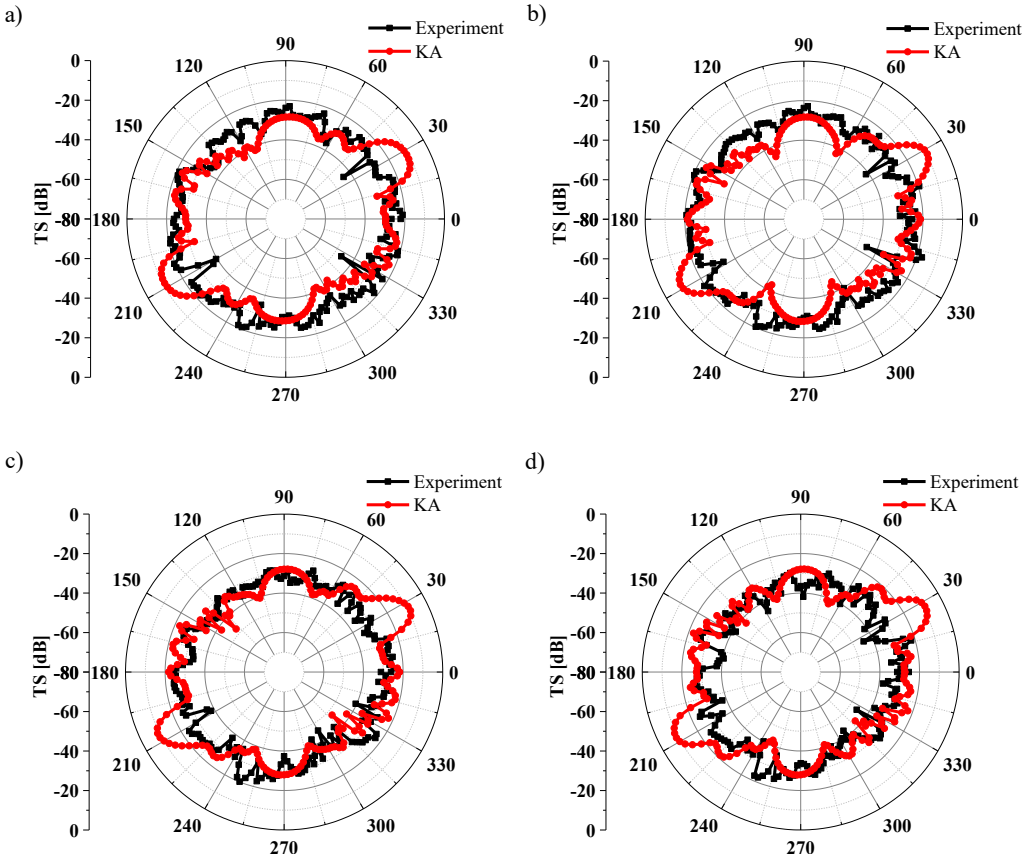

Fig. 16. The comparison results of the steel propeller TS at different frequencies: a) 14 kHz; b) 16 kHz; c) 18 kHz; d) 20 kHz.

4.3. The steel propeller scale model monostatic TS experimental data analysis

The experimental data underwent the Fourier transform, and the outcomes of at different frequencies were then compared with those derived from the KA method.

As shown in Fig. 16, the experimental results show a trend that closely matches the KA solutions, with the numerical values being largely consistent. This indicates that the KA method has a reliable degree of accuracy in predicting the TS of propellers. However, it is observed that there are some differences in the peak values near the strong intensity points at 30° and 210° between experimental results for the propeller and the KA solutions. These discrepancies could potentially be attributed to issues related to fabrication and suspension of the model.

5. Conclusion

This study initially employs an IA to determine the thickness of each discrete surface element. Subsequently, based on material parameters, OLTM is utilized to calculate the reflection coefficient of each discrete surface element. Finally, employing a coherent superposition approach, the scattered acoustic field of a single composite propeller blade is obtained. To streamline computations, a mesh topology cloning method is employed to predict the acoustic scattering characteristics of the entire composite propeller. Comparative analysis of the acoustic scattering characteristics of the composite propeller yielded the following key conclusions:

1) Compared to the traditional FEM, the KA method is shown to rapidly and accurately predict the high-frequency acoustic scattering characteristics of composite thin-plate models with spatially varying thickness.
2) For geometric models that exhibit rotational symmetry, complete multi-body models can be obtained by topologically cloning individual structures in the mesh. This method effectively predicts the acoustic scattering characteristics, with these typical structures displaying a consistent distribution pattern of rotational symmetry in their directivity diagrams of TS.
3) The propeller blade significantly affects the TS of the static composite propeller. An overall TS peak is observed when a considerable number of surface

elements on the propeller blade have an outward normal nearly parallel to the incident direction.

4) Compared to the acoustic scattering results from lake experiments, this study demonstrates that the applying the KA method to the isotropic steel propeller also ensures the high solution accuracy. This enhances the prediction accuracy of the stern direction acoustic scattering characteristics of underwater vehicles.

Acknowledgments

This work is sponsored and supported by the National Natural Science Fund of China (no. 52201397 and 52001211) and the Hunan Province Natural Science Fund (no. 2023JJ60544).

References

1. Cheng Z.K. *et al.* (2023), Observation of the rotational Doppler shift of a spinning object based on an acoustic vortex with a Fresnel-spiral zone plate, *Journal of Applied Physics*, **133**(11): 114502, doi: 10.1063/5.0141106.

2. Chu D., Stanton T.K. (2010), Statistics of echoes from a directional sonar beam insonifying finite numbers of single scatterers and patches of scatterers, *IEEE Journal of Oceanic Engineering*, **35**(2): 267–277, doi: 10.1109/JOE.2009.2037988.

3. Fan J., Tang W.L., Zhuo L.K. (2012), Planar elements method for forecasting the echo characteristics from sonar targets [in Chinese], *Journal of Ship Mechanics*, **16**(1): 171–180, doi: 10.3969/j.issn.1007-7294.2012.01.020.

4. Hu P. (2017), *Research on target strength of submarine sails made by sound-reflecting composites*, MSc. Thesis, China Ship Research and Development Academy.

5. Isakson M.J., Chotiros N.P. (2014), Finite element modeling of acoustic scattering from fluid and elastic rough interfaces, *IEEE Journal of Oceanic Engineering*, **40**(2): 475–484, doi: 10.1109/JOE.2014.2313060.

6. Islam F., Caldwell R., Phillips A.W., St John N.A., Prusty B.G. (2022), A review of relevant impact behaviour for improved durability of marine composite propellers, *Composites Part C: Open Access*, **8**: 100251, doi: 10.1016/j.jcomc.2022.100251.

7. Jiang B., Yu J., Li W., Chai Y., Gui Q. (2023), A coupled overlapping finite element method for analyzing underwater acoustic scattering problems, *Journal of Marine Science and Engineering*, **11**(9): 1676, doi: 10.3390/jmse11091676.

8. Jing J., Hu Y.F., Ding G.P. (2022), Simulation research on modal analysis of CFRP propeller, *Digital Manufacture Science*, **20**(1): 29–33.

9. Klausner N, Azimi-Sadjadi MR. (2014), Non-Gaussian target detection in sonar imagery using the multivariate laplace distribution, *IEEE Journal of Oceanic Engineering*, **40**(2): 452–464, doi: 10.1109/JOE.2014.2328211.

10. Kuo Y.-M., Lin H.-J., Wang C.-N. (2008), Sound transmission across orthotropic laminates with a 3D model, *Applied Acoustics*, **69**(11): 951–959, doi: 10.1016/j.apacoust.2007.08.002.

11. Kwon H.W., Hong S.Y., Song J.H. (2017), A study for acoustic target strength characteristics of submarines using Kirchhoff approximation, *Marine Technology Society Journal*, **51**(4): 52–58, doi: 10.4031/MTSJ.51.4.5.

12. Langdon S., Chandler-Wilde S.N. (2006), A wavenumber independent boundary element method for an acoustic scattering problem, *SIAM Journal on Numerical Analysis*, **43**(6): 2450–2477, doi: 10.1137/S0036142903431936.

13. Lavia E.F., Gonzalez J.D., Blanc S. (2019), Modeling high-frequency backscattering from a mesh of curved surfaces using Kirchhoff approximation, *Journal of Theoretical and Computational Acoustics*, **27**(04): 1850057, doi: 10.1142/S2591728518500573.

14. Li D. (2022), *Analysis of Composite Laminates: Theories and Their Applications*, Science Press, China.

15. Lin H.-J., Wang C.-N., Kuo Y.-M. (2017), Sound transmission loss across specially orthotropic laminates, *Applied Acoustics*, **68**(10): 1177–1191, doi: 10.1016/j.apacoust.2006.06.007.

16. Möller T., Trumbore B. (1997), Fast, minimum storage ray-triangle intersection, *Journal of Graphics Tools*, **2**(1): 21–28, doi: 10.1145/1198555.1198746.

17. Motley M.R., Liu Z., Young Y.L. (2009), Utilizing fluid–structure interactions to improve energy efficiency of composite marine propellers in spatially varying wake, *Composite Structures*, **90**(3): 304–313, doi: 10.1016/j.compstruct.2009.03.011.

18. Sabat R. *et al.* (2023), Low frequency sound isolation by a metasurface of Helmholtz ping-pong ball resonators, *Journal of Applied Physics*, **134**(14): 144502, doi: 10.1063/5.0160267.

19. Saffari A., Zahiri S.H., Ghanad N.K. (2023), Using SVM classifier and micro-Doppler signature for automatic recognition of sonar targets, *Archives of Acoustics*, **48**(1): 49–61, doi: 10.24425/aoa.2022.142909.

20. Sagar M.V., Venkaiah M., Sunil D. (2013), Static and dynamic analysis of composite propeller of ship using FEA, *International Journal of Engineering Research & Technology* (*IJERT*), **2**(7): 2587–2594, doi: 10.17577/IJERTV2IS70418.

21. Seybert A.F., Wu T.W., Wu X.F. (1988), Radiation and scattering of acoustic waves from elastic solids and

shells using the boundary element method, *The Journal of the Acoustical Society of America*, **84**(5): 1906–1912, doi: 10.1121/1.397156.

22. Tang W.L. (1993), Calculation of acoustic scattering of a nonrigid surface using physical acoustic method [in Chinese], *Acta Acustica*, **18**(1): 45–53, doi: 10.15949/j.cnki.0371-0025.1993.01.006.

23. Tucker J.D, Azimi-Sadjadi M.R. (2011), Coherence-based underwater target detection from multiple disparate sonar platforms, *IEEE Journal of Oceanic Engineering*, **36**(1): 37–51, doi: 10.1109/JOE.2010.2094230.

24. Uddin M.M., Hossen M.P., Jahan M.M., Islam M.I. (2021), Structural analysis of composite propeller of ship using FEM, [in:] *AIP Conference Proceedings*, **2324**(1): 030001, doi: 10.1063/5.0037760.

25. Vardhan D.H., Ramesh A., Reddy B.C.M. (2019), A review on materials used for marine propellers, *Materials Today*: *Proceedings*, **18**(7): 4482–4490, doi: 10.1016/j.matpr.2019.07.418.

26. Venås J.V., Kvamsdal T. (2020), Isogeometric boundary element method for acoustic scattering by a submarine, *Computer Methods in Applied Mechanics and Engineering*, **359**: 112670, doi: 10.1016/j.cma.2019.112670.

27. Yang F., Peng Z., Song H., Tang Y., Miao X. (2024), A hybrid finite element method – Kirchhoff approximation method for modeling acoustic scattering from an underwater vehicle model with Alberich coatings with periodic internal cavities, *Archives of Acoustics*, **49**(2): 209–219, doi: 10.24425/aoa.2024.148777.

28. Zhang X.G., Zhang J.F., Lyu S., Cao F., Li G.J., Wang N. (2020), Rapid method for large-scale target sound scattering calculation and experiment validation [in Chinese], *Journal of Ship Mechanics*, **24**(3): 409–418.

29. Zhu X.C. (2020), *Parametric modeling and CNC machining of ship propeller*, MSc. Thesis, Tianjin, Tiangong University.